Journal of Wind Engineering & Industrial Aerodynamics 219 (2021) 104803

Contents lists available at ScienceDirect

Journal of Wind Engineering & Industrial Aerodynamics

journal homepage: www.elsevier.com/locate/jweia

Another look at rotational sampling of atmospheric turbulence with focus on the transference of energy from different frequency intervals of the Eulerian spectrum to the rotational spectrum

A. Cuerva-Tejero *, M. Rodríguez-Correa, C. Gallego-Castillo, O. Lopez-Garcia, S. Ávila-Sánchez, R. Fernández-Aldama

Aircraft and Space Vehicles Department, Universidad Politécnica de Madrid, Plaza Cardenal Cisneros 3, 28040 Madrid, Spain

ARTICLE INFO

Keywords:
Rotational sampling
Wind turbine
Turbulence

ABSTRACT

Rotational sampling is of paramount importance in the loading of wind turbine blades due to wind turbulence We revisit the classical model of rotational sampling of the longitudinal component of a statistically stationary, homogeneous, isotropic turbulent velocity field experienced by a point rotating in a plane perpendicular to the mean velocity. As is well known, this is the simplest frame work, since it allows to determine the non-dimensional rotational spectrum in terms of the non-dimensional frequency and only two more non dimensional parameters, the non dimensional radial position of the rotating point and the non dimensional rotational speed. We systematize the parametric analysis of the rotational spectrum proposed independently by Connel in 1981 and Kristensen et al. in 1982, in terms of the aforementioned two non dimensional parameters. We propose a quantification of the transference of energy from different frequency intervals of the Eulerian spectrum to the rotational spectrum. We verify that regions of the Eulerian spectrum corresponding to different frequency intervals are transformed into contributions to the rotational spectrum that expand to the whole frequency range without preserving the variance. Certain frequency intervals of the Eulerian spectrum can lead to negative contributions to the rotational spectrum along certain frequency ranges.

1. Introduction

Rotational sampling of atmospheric turbulence by wind turbine blades is a well known phenomenon since the pioneering work of Rosenbrock (1955), who established the theoretical basis for the rotational sampling of turbulence in a vertical plane perpendicular to the mean wind speed. The first round of systematic experiments on this phenomenon were initiated by Verholek (1978) and the works of Connell (1981) and Kristensen and Frandsen (1982), Kristensen (1983) consolidated the theoretical framework to study the rotational sampling of statistically stationary, homogeneous and isotropic turbulence for horizontal axis wind turbines. A similar mathematical frame work was applied to the study of linear sampling of turbulence in the context of moving ground vehicles in Cooper (1984). These results are still being used as a reference in recent studies on the wind spectra experienced by a moving point (Su et al., 2020).

Connell (1982) outlined different turbulence characteristics encountered by a rotating blade compared to those measured by a stationary anemometer. He related these differences to the distortion of the spectrum of the observed turbulence in several sub-ranges of frequency. In Connell's words, the mid frequency region is depleted and the removed energy is transferred to the high frequency end of the spectrum. He succeeded in applying a Statistically Stationary, Homogeneous and Isotropic turbulence model (SSHIT) to identify the two non dimensional parameters influencing this distortion process. These two non dimensional parameters are the non dimensional radial position of the rotating point, $\mathring{\rho}$, defined as $\mathring{\rho} = \rho L^{-1}$ where ρ is the radial position and L is the characteristic length scale of the energy spectrum (Pope, 2000) and the non dimensional rotational speed, $\mathring{\Omega}$, defined as $\mathring{\Omega} = \Omega L U_1^{-1}$, where Ω is the rotational speed and U_1 the mean wind speed, see Fig. 1.

Experimental studies on the rotational sampling phenomenon in a horizontal plane, which is relevant for vertical axis wind turbines, were also initiated at that time (Akins, 1983; Sandborn and Connell, 1984; George, 1984), reaching qualitatively similar conclusions. However, the development of theoretical models for such condition

* Corresponding author.
E-mail address: alvaro.cuerva@upm.es (A. Cuerva-Tejero).

https://doi.org/10.1016/j.jweia.2021.104803
Received 6 May 2021; Received in revised form 6 October 2021; Accepted 6 October 2021
Available online 20 October 2021

Symbols

f	Frequency.
$\mathring{f}$	Non dimensional frequency.
$\mathring{f}_a$	Lower limit of a non dimensional frequency interval.
$\mathring{f}_b$	Upper limit of a non dimensional frequency interval.
$\mathring{f}_i$	Center of a non dimensional frequency interval.
$f(r)$	Non dimensional longitudinal correlation.
$f_{ab}(r)$:	Non dimensional longitudinal correlation corresponding to an interval of non dimensional longitudinal wave numbers $[\mathring{k}_a, \mathring{k}_b]$.
$F_i(k_1)$	One dimensional spectrum corresponding to a velocity component u_i.
$\mathring{f}_{n\Omega}$	Non dimensional frequency corresponding to n−multiples of the non dimensional rotational speed.
$\mathring{f}_{n\Omega}\mathring{S}_u^{n\Omega}$	Normalized spectrum at non dimensional frequency $\mathring{f}_{n\Omega}$.
$g(r)$	Non dimensional transverse correlation.
$g_{ab}(r)$	Non dimensional transverse correlation corresponding to an interval of non dimensional longitudinal wave numbers $[\mathring{k}_a, \mathring{k}_b]$.
k	Magnitude of the vector wave number, longitudinal component of the vector wave number when indicated. k_1 : Longitudinal component of the vector wave number.
$\mathring{k}$	Magnitude of the non dimensional vector wave number. Longitudinal component of the non dimensional vector wave number when indicated.
L	Length scale of the three dimensional energy spectrum.
r	Magnitude of the separation vector.
$\mathbf{r}$	Separation vector.
$\mathring{r}$	Magnitude of the non dimensional separation vector.
$\mathring{\mathbf{r}}$	Non dimensional separation vector.
$R_{ij}(\mathbf{r})$	Correlation tensor.
$\mathring{R}_{ij}(\mathring{\mathbf{r}})$	Non dimensional correlation tensor.
$\mathring{S}_u$	Non dimensional Eulerian spectrum.
$\mathring{S}_u^{\Omega}$	Non dimensional rotational spectrum.
$\mathring{S}_{u_{ab}}^{\Omega}$	Non dimensional interval limited rotational spectrum.
$S_u^{\Omega,2}$	Two sided rotational spectrum.
t	time.
u_j	Fluctuation of a wind velocity component.
U_1, U	Mean wind speed.
$\mathbf{x}$	Position vector.
α	Random index.
λ_ρ	Radial section speed ratio.
Ω	Rotational speed.
$\mathring{\Omega}$	Non dimensional rotational speed.
ρ	Radial position.
$\mathring{\rho}$	Non dimensional radial position.
σ_0^2	Isotropic variance.
$\mathring{\sigma}_{u^\Omega}^2$	Non dimensional rotational variance.
$\mathring{\sigma}_u^2\Big\vert_a^b$	Non dimensional variance associated to the frequency interval $[\mathring{f}_a, \mathring{f}_b]$ of the Eulerian spectrum.
$\mathring{\sigma}_{u_{ab}^\Omega}^2$	Non dimensional interval limited rotational variance (associated to the non dimensional interval limited rotational spectrum $\mathring{S}_{u_{ab}}^{\Omega}$).
$\mathring{\sigma}_{u^\Omega}^2\Big\vert_a^b$	Non dimensional rotational variance associated to the frequency interval $[\mathring{f}_a, \mathring{f}_b]$ of the non dimensional rotational spectrum $\mathring{S}_u^{\Omega}$.
$\mathring{\sigma}_{u_{ab}^\Omega}^2\Big\vert_a^b$	Non dimensional interval limited rotational variance associated to the frequency interval $[\mathring{f}_a, \mathring{f}_b]$ of the non dimensional interval limited rotational spectrum $\mathring{S}_{u_{ab}}^{\Omega}$.

required some more time to appear due to their higher difficulty. As concluded in Connell (1981) and Kristensen and Frandsen (1982), when rotational sampling takes place in a plane perpendicular to the mean wind velocity, if the random process associated to the longitudinal velocity component is statistically stationary, the rotationally sampled longitudinal velocity component is also a stationary random process, and therefore the rotational time correlation does not depend on time. This is not the case when the rotational sampling process takes place in a horizontal plane. In this situation, the resulting rotationally sampled longitudinal velocity component constitutes a cyclostationary random process (Napolitano, 2012) and the corresponding rotational correlation and spectrum present time periodicity. This situation is of particular interest for helicopter rotors in forward flight and it has been analyzed in detail by different authors (Costello et al., 1992; Riaz et al., 1993; Gaonkar, 2008).

The theoretical developments of Rosenbrock, Connel and Kristensen, were the basis for a number of experimental works in the 1980's (Connell and Powell, 1989; Powell and Connell, 1987). In George and Connell (1984) one of the pioneering experimental analysis on the rotational sampling phenomenon in connection to wind turbine blade fatigue loading was presented. In that study, a large array of fixed anemometers located two rotor diameters upwind of a 200-kW horizontal-axis wind turbine was used to establish a quantitative comparison between the rotationally sampled wind input and blade bending moment response. The main conclusions of this study were summarized in Connell and George (1987). In Hardesty and Weber (1986) and Connell and Morris (1989), the rotational sampling in a vertical plane perpendicular to the mean wind velocity was investigated by means of lidar techniques. At the end of the decade, the rotational sampling of turbulence was considered among the relevant loading factors of wind turbines (Connell, 1988).

The 1990's lead to some new theoretical contributions such as Dragt (1990), as well as an increased interest on the influence of the phenomenon in the fatigue loading of wind turbines. In Spera (1995) and Connell (1995), the rotational sampling was identified as the driving factor of higher fatigue loads associated to the blade flap-wise bending moment, not explained by the Eulerian spectrum of wind velocity. Finally, the consequences of rotational sampling on wind turbine loading were widely evidenced and the phenomenon was included in textbooks (Burton et al., 2001).

The capability for reproducing rotationally sampled spectra of the numerical generation algorithms for simulating wind velocity time series from statistical descriptions of turbulence (applied to wind turbine aeroelastic calculations) were put to the tests. In Powell and Connell (1986), three numerical simulation methods were investigated.

In Petersen et al. (1994), the Veers (1988) and Mann (1994) methods for numerical synthesis of wind velocity time series were compared in terms of their capability of reproducing the relative wind velocity and angle of attack of a wind turbine rotating blade section. Two interpolation techniques to increase the spatial resolution of synthetic turbulent wind fields in the rotor plane of wind turbines were compared in Fluck and Crawford (2016), by establishing the differences in the rotational spectra obtained from both interpolated wind fields.

Full scale experiments on rotational sampling have continued until our days. In Simley and Pao (2013) and Sekar et al. (2020) hub mounted lidars were used to obtain rotationally sampled wind fields. The investigation of the specific effects of rotational sampling on wind turbine fatigue has also continued. In Murtagh et al. (2005), this effect was analyzed using a reduced dynamic model of a wind turbine. The authors presented an attempt to quantify the amount of variance accounted for by each $n\Omega$ peak, $n \in \mathbb{N}$, of the rotational spectrum, considering the influence of the blade section radial position. In Eliassen et al. (2015), the rotational sampling of turbulence was analyzed in the context of increasing size wind turbines. In Elgammi et al. (2020) a Blade Element Momentum (BEM) model was applied to predict the aerodynamic loads for yawed rotors operating in natural flow conditions with special focus on the rotational sampling effect. In Bei et al. (2018) the authors concluded on the relevance of the rotational sampling of turbulence in the characterization of flutter of wind turbine blades.

New models of numerical generation of wind velocity fields, including rotational sampling effects, have being proposed in the recent years. In Sørensen et al. (2002), a wind field model for wind farms including rotational sampling effects has been proposed. In Burlibaşa and Ceangă (2013), a filter based technique was combined with a classical model of the rotational spectrum. In Chen et al. (2015), a combination of Proper Orthogonal Decomposition of wind modes and a classical modeling of the rotational spectrum (Powell and Connell, 1987) was developed to generate the wind fields required for the aeroelastic simulation of a wind turbine. The work presented in Chen et al. (2020) is of special interest for the analysis proposed in this paper since the authors propose an analytic formulation of the rotationally sampled spectrum based on a frequency–wave number description of the wind velocity, and they succeed in expressing the two-sided rotational spectrum by means of three contributions, with two of them clearly revealing how much of the energy of the Eulerian spectrum is shifted to regions of frequencies around the rotational peaks $\pm n\Omega(2\pi)^{-1}$, $n \in \mathbb{N}$. Similar techniques of numerical generation of wind velocity fields, including linear sampling effects, have been applied in the dynamic analysis of moving ground vehicles (Baker, 2010).

The article is structured as follows: In Section 2, we include the essential elements of the SSHIT statistical description. In Section 3, we describe the classical rotational sampling approach in a vertical plane. We extend the parametric analysis of the non dimensional rotational spectrum $\mathring{S}_u^{\Omega}(\mathring{f};\mathring{\rho},\mathring{\Omega})$, where the non dimensional frequency $\mathring{f}$ is defined as $\mathring{f} = fLU_1^{-1}$ where f is frequency, proposed by Connell (1981) and Kristensen and Frandsen (1982) for specific values of the non dimensional radial position $\mathring{\rho}$ and non dimensional rotational speed $\mathring{\Omega}$, (the radial section speed ratio $\lambda_\rho = \mathring{\Omega}\mathring{\rho}$, instead of $\mathring{\Omega}$, is alternatively used) to intervals of both parameters. The non dimensional rotational spectrum is defined as $\mathring{S}_u^{\Omega}(\mathring{f};\mathring{\rho},\mathring{\Omega}) = L^{-1}U_1\sigma_0^{-2}S_u^{\Omega}(f = \mathring{f}U_1L^{-1};\rho = \mathring{\rho}L,\Omega = \mathring{\Omega}U_1L^{-1})$, where σ_0^2 is the isotropic variance. We analyze different characteristics of $\mathring{S}_u^{\Omega}(\mathring{f};\mathring{\rho},\mathring{\Omega})$ and revisit some classical results.

In Section 4, we quantify how the different frequency intervals of the non dimensional Eulerian spectrum, $\mathring{S}_u(\mathring{f})$, $\mathring{f} \in [\mathring{f}_a,\mathring{f}_b]$, contribute to the non dimensional rotational spectrum $\mathring{S}_u^{\Omega}(\mathring{f};\mathring{\rho},\mathring{\Omega})$. These contributions are defined as the non dimensional interval limited rotational spectrum, $\mathring{S}_{u_{ab}}^{\Omega}(\mathring{f};\mathring{\Omega},\mathring{\rho})$, $\mathring{f} \in [0,\infty)$. We prove that the non dimensional variance $\mathring{\sigma}_u^2\big|_a^b = \sigma_u^2\big|_a^b/\sigma_0^2$, which is the non dimensional variance corresponding to the Eulerian spectrum $\mathring{S}_u(\mathring{f})$, $\mathring{f} \in [\mathring{f}_a,\mathring{f}_b]$, differs, in general, from the non dimensional rotational variance $\mathring{\sigma}_{u_{ab}^{\Omega}}^2$, which is the variance corresponding to $\mathring{S}_{u_{ab}}^{\Omega}(\mathring{f};\mathring{\Omega},\mathring{\rho})$, $\mathring{f} \in [0,\infty)$. We analyze the ratio $\mathring{\sigma}_{u_{ab}^{\Omega}}^2 / \mathring{\sigma}_u^2\big|_a^b$ for different frequency intervals $[\mathring{f}_a,\mathring{f}_b]$ of the Eulerian spectrum and for different values of parameters λ_ρ and $\mathring{\rho}$. We reveal that the variance change is due to the different contribution of the longitudinal correlation and transverse correlation in the rotational correlation. This different contribution depends on the considered frequency interval of the Eulerian spectrum $[\mathring{f}_a,\mathring{f}_b]$, and the radial section speed ratio λ_ρ. We also quantify the contributions of the non dimensional interval limited rotational spectra to the 1Ω and 2Ω rotational peaks.

Finally we establish the conclusions of our analysis in Section 5.

2. Elements of homogeneous, stationary and isotropic turbulence

The strictly necessary elements on the statistical description of statistically stationary, homogeneous, isotropic turbulence, required to support our developments, are included for sake of clarity. We consider the random process which represents the turbulent velocity field with components $\tilde{u}_i(\mathbf{x},t;\alpha) = U_i\delta_{1i} + u_i(\mathbf{x},t;\alpha)$ defined in the Cartesian reference system x_i, $i = 1,2,3$. δ_{ij} is the Kronecker's δ, $U_i\delta_{1i} = U_1$ is the mean wind velocity and $u_i(\mathbf{x},t;\alpha)$ is the fluctuation wind velocity field. Vector $\mathbf{x}$ represents the position in space, t is time and α is a random index which identifies the realization of the random process. As it is well known (Durbin and Reif, 2011), the two point correlation tensor is defined as

$$\overline{u_i^*(\mathbf{x},t;\alpha)u_j(\mathbf{x}+\mathbf{r},t;\alpha)} = R_{ij}(\mathbf{r},t),$$

where * stands for complex conjugate. The correlation tensor is independent of time due to statistical stationarity. Therefore, the two points correlation tensor is written $R_{ij}(\mathbf{r})$ from now on, and only depends on the separation vector, $\mathbf{r}$, due to homogeneity.

In SSHI turbulence (von Karman, 1948) the two points correlation tensor can be expressed in terms of a single scalar non dimensional function, the longitudinal non dimensional correlation function $f(r)$ as

$$R_{ij}(\mathbf{r}) = \sigma_0^2\left[\frac{f(r)-g(r)}{r^2}r_ir_j + g(r)\delta_{ij}\right], \tag{1}$$

where $g(r)$ is the non dimensional transverse correlation function given by

$$g(r) = \frac{1}{2r}\frac{\mathrm{d}}{\mathrm{d}r}\left[r^2f(r)\right], \tag{2}$$

being $\mathbf{r} = r_i$, $i = 1,2,3$, and $r = |\mathbf{r}|$. In this paper, we use the von Karman formulation (Durbin and Reif, 2011; von Karman, 1948) for $f(r)$, being

$$f(r) = \frac{2}{\Gamma(\gamma-1/2)}\left(\frac{r}{2L}\right)^{\gamma-1/2}K_{\gamma-1/2}\left(\frac{r}{L}\right),$$

where K_x is the modified Bessel function of the second kind of order x and Γ is the Gamma function. We use, in what follows, the value γ=5/6 proposed by von Karman, accordingly to Kolmogorov $-5/3$ energy spectrum (Pope, 2000). Using the von Karman formulation for $f(r)$ into Eq. (2), the function $g(r)$ results

$$g(r) = f(r) - \frac{2}{\Gamma(\gamma-1/2)}\left(\frac{r}{2L}\right)^{\gamma+1/2}K_{\gamma-3/2}\left(\frac{r}{L}\right).$$

The one-dimensional spectra in terms of longitudinal component of the wavenumber vector, k_1, corresponding to the longitudinal velocity component, $F_1(k_1)$ and the transverse velocity components, $F_{2,3}(k_1)$ are

$$F_1(k_1) = \frac{1}{\sqrt{\pi}}\frac{\Gamma(\gamma)}{\Gamma(\gamma-1/2)}\frac{\sigma_0^2L}{\left[1+(k_1L)^2\right]^\gamma},$$

$$F_{2,3}(k_1) = \left[\frac{1}{2} + \frac{\gamma(k_1L)^2}{1+(k_1L)^2}\right]F_1(k_1).$$

The functions $f(r)$ and $F_1(k_1)$ on the one side and $g(r)$ and $F_{2,3}(k_1)$ on the other, are Fourier pairs, that is

$$f(r) = \int_{-\infty}^{\infty} F_1(k_1)\exp(ik_1 r)\mathrm{d}r = 2\int_0^{\infty} F_1(k_1)\cos(k_1 r)\mathrm{d}r, \tag{3}$$

$$g(r) = \int_{-\infty}^{\infty} F_{2,3}(k_1)\exp(ik_1 r)\mathrm{d}r = 2\int_0^{\infty} F_{2,3}(k_1)\cos(k_1 r)\mathrm{d}r, \tag{4}$$

where, to obtain the right-most side of Eqs. (3) and (4) it has been considered that $F_i(k_1)$, $i = 1,2,3$, are even functions of k_1. The non dimensional correlations $f(r)$ and $g(r)$ are functions of the non dimensional separation $\mathring{r} = rL^{-1}$. The non dimensional counterparts of $F_i(k_1)$ functions are defined by $\mathring{F}_i(k_1 L) = L^{-1}\sigma_0^{-2}F_i(k_1 = \mathring{k}_1 L^{-1})$. This is one of the advantages of using the SSHI turbulence framework, functions $f(\mathring{r})$ and $g(\mathring{r})$ depend on a single non dimensional parameter, $\mathring{r}$, and the non dimensional one-dimensional spectra $\mathring{F}_i$ also depend on a single non dimensional parameter $\mathring{k}_1 = k_1 L$.

It can be easily proved (Taylor, 1938) that the Taylor's Frozen Turbulence Hypothesis (TFTH) allows one to relate the one-dimensional spectra in terms of the wave number $F_i(k_1)$ with the one-sided spectra of a velocity component fluctuation u_i, measured at a fixed point as

$$S_{u_i}(f) = 4\pi U_1^{-1}F_i(k_1 = 2\pi U_1^{-1}f), \tag{5}$$

where it has been considered that

$$\sigma_0^2 = \int_{-\infty}^{\infty} F_i(k_1)\mathrm{d}k_1 = \int_0^{\infty} S_{u_i}(f)\mathrm{d}f.$$

Expression (5) can be rewritten in terms of the corresponding non dimensional functions as

$$\frac{U_1}{L}\sigma_0^{-2}S_{u_i}(f = \mathring{f}U_1 L^{-1}) = \mathring{S}_{u_i}(\mathring{f}) = 4\pi\mathring{F}_i(\mathring{k}_1 = 2\pi\mathring{f}).$$

For sake of simplicity U_1, u_1 and k_1 will be written as U, u and k in what follows. Note that the non dimensional two point correlation tensor is $\mathring{R}_{ij}(\mathring{\mathbf{r}}) = \sigma_0^{-2}R_{ij}(\mathbf{r} = \mathring{\mathbf{r}}L)$.

3. Classic rotational sampling approach in a vertical plane

Following Connell (1981) and Kristensen and Frandsen (1982), when a point located at a distance ρ from a rotating axis describes a circular trajectory contained in a plane perpendicular to the mean wind velocity $U\mathbf{e}_1$, with constant rotational speed Ω, the correlation of the longitudinal velocity components at times t and $t+\tau$ corresponds to the correlation between the fluctuation u at point $\mathbf{x}_A$ and time t, and the fluctuation u at point $\mathbf{x}_B$ and time $t+\tau$, see Fig. 1. The TFTH establishes that $u(\mathbf{x}_B, t+\tau, \alpha)$ equals the fluctuation $u(\mathbf{x}_C, t; \alpha)$ with $\mathbf{x}_C = \mathbf{x}_B - U\tau\mathbf{e}_1$ and therefore is

$$\overline{u^*(\mathbf{x}_A, t; \alpha)u(\mathbf{x}_B, t+\tau; \alpha)} = \overline{u^*(\mathbf{x}_A, t; \alpha)u(\mathbf{x}_C, t; \alpha)}. \tag{6}$$

The space–time correlation (6) is easily expressed from the two point correlation tensor (1) as

$$\sigma_0^{-2}R_u^{\Omega}(\tau; \Omega, \rho) = \left[\frac{f(r) - g(r)}{r^2}r_1^2 + g(r)\right], \tag{7}$$

where $i = j = 1$ has been considered, $r_1 = -U\tau$ and

$$r = \left\{(U\tau)^2 + \left[2\rho\sin\left(\frac{\Omega\tau}{2}\right)\right]^2\right\}^{1/2}. \tag{8}$$

The superscript Ω in expression (7) denotes "rotational". The corresponding two-sided (superscript "2") rotational (superscript "Ω") spectrum in terms of radian frequency ω is the Fourier pair of $R_u^{\Omega}(\tau; \Omega, \rho)$ given by

$$\sigma_0^{-2}S_u^{\Omega,2}(\omega; \Omega, \rho) = \sigma_0^{-2}\frac{1}{2\pi}\int_{-\infty}^{\infty} R_u^{\Omega}(\tau; \Omega, \rho)\exp(-i\omega\tau)\mathrm{d}\tau.$$

We use, from now on, the one-sided rotational spectrum in terms of frequency, $S_u^{\Omega}(f)$, which is

$$\sigma_0^{-2}S_u^{\Omega}(f; \Omega, \rho) = 4\sigma_0^{-2}\int_0^{\infty} R_u^{\Omega}(\tau; \Omega, \rho)\cos(2\pi f\tau)\mathrm{d}\tau,$$

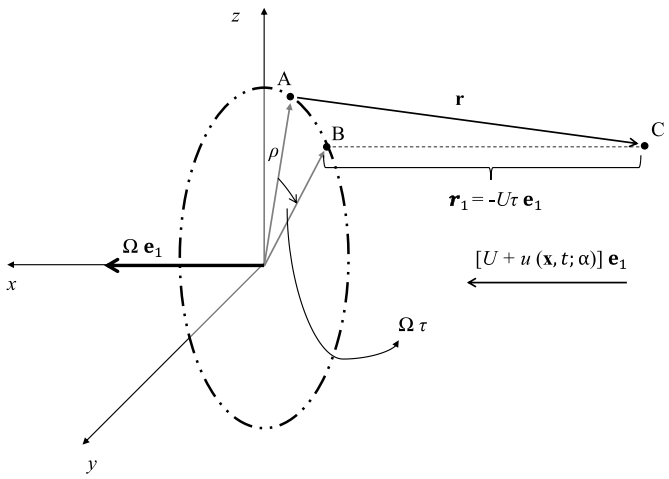

Fig. 1. Rotational sampling scheme corresponding to a point describing a circular trajectory with radius ρ and with rotational speed Ω, perpendicular to the mean wind velocity $U\mathbf{e}_1$ and immersed in a turbulent velocity field $[U + u(\mathbf{x}, t; \alpha)]\mathbf{e}_1$.

where it has been taken into account that the variance of the velocity fluctuation experienced by the rotating point, defined as rotational variance is

$$\sigma_{u^{\Omega}}^2 = \int_{-\infty}^{\infty} S_u^{\Omega,2}(\omega; \Omega, \rho)\mathrm{d}\omega = \int_0^{\infty} S_u^{\Omega}(f; \Omega, \rho)\mathrm{d}f. \tag{9}$$

and that from expression (7) the symmetry relation $R_u^{\Omega}(\tau; \Omega, \rho) = R_u^{\Omega}(-\tau; \Omega, \rho)$ holds.

The rotational variance is, from expressions (7) and (8),

$$\sigma_{u^{\Omega}}^2 = \lim_{\tau\to 0} R_u^{\Omega}(\tau; \Omega, \rho) = \sigma_0^2\left[\frac{f(0) - g(0)}{\lambda_{\rho}^2 + 1} + g(0)\right] = \sigma_0^2, \tag{10}$$

since $f(0) = g(0) = 1$. Clearly, the described rotational sampling process does not provoke any modification of the original variance as stated in Connell (1981) and Kristensen and Frandsen (1982) and verified, in a more general case, in Chen et al. (2020).

As in Connell (1981) and Kristensen and Frandsen (1982), in what follows we use the non dimensional parameters $\mathring{\rho} = \rho L^{-1}$ and $\mathring{\Omega} = \Omega L U^{-1}$. The non dimensional rotational correlation is

$$\begin{aligned}\mathring{R}_u^{\Omega}(\mathring{\tau}; \mathring{\Omega}, \mathring{\rho}) &= \sigma_0^{-2}R_u^{\Omega}(\tau = \mathring{\tau}LU^{-1}; \Omega = \mathring{\Omega}UL^{-1},\\ \rho = \mathring{\rho}L) &= \left[\frac{f(\mathring{r}) - g(\mathring{r})}{\mathring{r}^2}\mathring{r}_1^2 + g(\mathring{r})\right],\end{aligned} \tag{11}$$

being

$$\mathring{r}_1 = -\mathring{\tau} = -\tau UL^{-1},$$

$$\mathring{r} = \left\{\mathring{\tau}^2 + \left[2\mathring{\rho}\sin\left(\frac{\mathring{\Omega}\mathring{\tau}}{2}\right)\right]^2\right\}^{1/2}, \tag{12}$$

and the non dimensional rotational spectrum $\mathring{S}_u^{\Omega}(\mathring{f}; \mathring{\Omega}, \mathring{\rho})$ is obtained from the non dimensional rotational correlation given in (11) as

$$\mathring{S}_u^{\Omega}(\mathring{f}; \mathring{\Omega}, \mathring{\rho}) = 4\int_0^{\infty}\mathring{R}_u^{\Omega}(\mathring{\tau}; \mathring{\Omega}, \mathring{\rho})\cos(2\pi\mathring{f}\mathring{\tau})\mathrm{d}\mathring{\tau}.$$

Connell (1981) and Kristensen and Frandsen (1982) introduced the radial section speed ratio $\lambda_{\rho} = \Omega\rho U^{-1} = \mathring{\Omega}\mathring{\rho}$ as an alternative non dimensional parameter. The parameter λ_{ρ} evaluated at the rotor radius takes typical values for small wind turbine rotors $\lambda_{\rho} \simeq [0, 4]$ and for large wind turbine rotors $\lambda_{\rho} \simeq [0, 10]$.

Since from now on we use only non dimensional parameters, frequencies, variances, correlations and spectra, as above defined, we refer to $\mathring{\rho}$, $\mathring{\Omega}$ and $\mathring{f}$ simply as radial position, rotational speed and frequency, respectively. The forms $\mathring{\sigma}_u^2$, $\mathring{R}_u$ and $\mathring{S}_u$ are named simply as

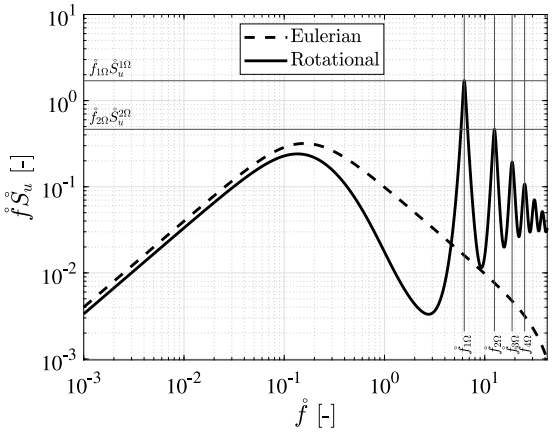

Fig. 2. Normalized Eulerian spectrum and normalized rotational spectrum for radial position $\mathring{\rho} = 0.25$ and rotational speed $\mathring{\Omega} = 39.3$ ($\mathring{f}_{1\Omega} = 6.25$), radial section speed ratio $\lambda_\rho = 9.8$. The non dimensional frequencies $\mathring{f}_{n\Omega} = (2\pi)^{-1} n\mathring{\Omega}$, $n = 1,2,3,4$, are indicated in the figure. The values of the normalized rotational spectrum at $\mathring{f}_{1\Omega}$ and $\mathring{f}_{2\Omega}$, $\mathring{f}_{1\Omega}\mathring{S}_u^{1\Omega}$ and $\mathring{f}_{2\Omega}\mathring{S}_u^{2\Omega}$, respectively, are also represented in the figure.

Table 1
Characteristic values $\mathring{\rho}$ and $\mathring{\Omega}$ ($\mathring{f}_{1\Omega}$), or $\mathring{\rho}$ and λ_ρ of three wind turbines with different scales relative to the turbulence length scale L. Small Size, Medium Size and Large Size Wind Turbines: SSWT, MSWT and LSWT respectively. The MSWT is described in section 5.7.5 of Burton et al. (2001).

Label	$\mathring{\rho}$	$\mathring{\Omega}$	$\mathring{f}_{1\Omega}$	λ_ρ
SSWT	0.04	107	17	4.3
MSWT (Burton et al., 2001)	0.28	28	4.46	7.8
LSWT (Jonkman et al., 2009)	0.64	12.7	2	8.1

variances, correlations and spectra. Finally, the product $\mathring{f}\mathring{S}_u$ is referred as normalized spectra. As an example of rotational spectrum, figure 13 from Connell (1982) is reproduced in Fig. 2 to show the characteristic shifting of energy and the appearance of the rotational peaks. The frequencies $\mathring{f}_{n\Omega} = (2\pi)^{-1} n\mathring{\Omega}$, $n = 1,2,3,4$, as well as the values of the normalized rotational spectrum at frequencies $\mathring{f}_{1\Omega}$ and $\mathring{f}_{2\Omega}$ are identified in the figure. Note that we use the notation $\mathring{S}_u^{n\Omega} = \mathring{S}_u^{\mathring{\Omega}}(\mathring{f}_{n\Omega})$.

Connell (1981, 1982) proposed an analysis of the rotational spectrum $\mathring{S}_u^{\Omega}(\mathring{f};\mathring{\Omega},\mathring{\rho})$ for some values of the parameters $\mathring{\rho}$ and $\mathring{\Omega}$, or $\mathring{\rho}$ and λ_ρ. We extend now this parametric analysis to intervals of such parameters. First, we present the value of the normalized rotational spectrum $\mathring{f}\mathring{S}_u^{\Omega}$ and the ratio $\mathring{S}_u^{\Omega}/\mathring{S}_u$, both at frequency $\mathring{f}_{1\Omega}$, in Fig. 3. In both subfigures, the lines $\lambda_\rho = \mathring{\Omega}\mathring{\rho} = 2\pi\mathring{f}_{1\Omega}\mathring{\rho}$ have been plotted for different $\mathring{f}_{1\Omega}$ values.

Three wind turbines cases (small, medium and large size; SSWT, MSWT and LSWT respectively), whose characteristic values are described in Table 1, are considered in this parametric study. The regions of values $\mathring{\rho} - \lambda_\rho$ corresponding to the blade sections of these wind turbines are also plotted by means of colored areas, for the typical operational range of such wind turbines. The specific $\mathring{\rho}$ and λ_ρ values for the blade tip section and rated rotational speed of the wind turbines under study are also identified in the figure. Fig. 3*b* eases the precise quantification of some classical results. For instance, the region $\mathring{\rho} - \lambda_\rho$ where the ratio of spectra is $\mathring{S}_u^{1\Omega}/\mathring{S}_u(\mathring{f}_{1\Omega}) > 1$, indicating the appearance of the rotational peak at $\mathring{f}_{1\Omega}$ is clearly revealed. For the same ratio, i.e. $\mathring{S}_u^{1\Omega}/\mathring{S}_u(\mathring{f}_{1\Omega}) = 3$, the first rotational peak requires much higher rotational speed ($15 \lesssim \mathring{f}_{1\Omega} \lesssim 17$) to appear for SSWTs (i.e $\mathring{\rho} \lesssim 0.04$) than for LSWTs ($\mathring{\rho} \lesssim 0.64$, $0.9 \lesssim \mathring{f}_{1\Omega} \lesssim 2$). Obviously, the value of the normalized rotational spectrum $\mathring{f}_{1\Omega}\mathring{S}_u^{1\Omega}$ is smaller for the SSWT ($\mathring{f}_{1\Omega}\mathring{S}_u^{1\Omega} \simeq 0.1$) than for the LSWT ($\mathring{f}_{1\Omega}\mathring{S}_u^{1\Omega} \simeq 0.4$), see Fig. 3*a*.

The values of the normalized rotational spectrum at frequency $\mathring{f}_{2\Omega}$ and the magnitude of the second rotational peak relative to the magnitude of the first rotational peak, defined as the ratio $\mathring{f}_{2\Omega}\mathring{S}_u^{2\Omega}/(\mathring{f}_{1\Omega}\mathring{S}_u^{1\Omega})$, are presented in Fig. 4 as functions of parameters $\mathring{\rho}$ and λ_ρ. The magnitude of the second rotational peak increases along constant $\mathring{f}_{1\Omega}$ lines as $\mathring{\rho}$ increases, as in the case of the first rotational peak. The ratio $\mathring{f}_{2\Omega}\mathring{S}_u^{2\Omega}/(\mathring{f}_{1\Omega}\mathring{S}_u^{1\Omega})$ changes along constant $\mathring{f}_{1\Omega}$ lines as $\mathring{\rho}$ increases, meaning that the ratio of the energy shifted to $\mathring{f}_{2\Omega}$ and $\mathring{f}_{1\Omega}$ changes as the radial position changes.

4. Energy shifting from different frequency intervals

Our interest in this section is to quantify how the energy of the Eulerian spectrum $\mathring{S}_u(\mathring{f})$ from specific frequency intervals $\mathring{f} \in [\mathring{f}_a, \mathring{f}_b]$ is distributed or concentrated by the rotational sampling process in the rotational spectrum $\mathring{S}_{u_{ab}}^{\Omega}(\mathring{f};\mathring{\Omega},\mathring{\rho})$ along the whole frequency interval $\mathring{f} \in [0,\infty)$. $\mathring{S}_{u_{ab}}^{\Omega}$ is referred to as the "interval limited" rotational spectrum.

We apply the TFTH to relate the longitudinal component of the vector wave number and frequency in non dimensional form by $\mathring{k} = 2\pi\mathring{f}$. The longitudinal and transverse correlation functions, $f_{ab}(\mathring{r})$ and $g_{ab}(\mathring{r})$, associated to a frequency interval $[\mathring{f}_a, \mathring{f}_b]$ with $\mathring{f}_b > \mathring{f}_a \geqslant 0$, corresponding to the wave number interval $[\mathring{k}_a, \mathring{k}_b]$, result from expressions (3) and (4)

$$f_{ab}(\mathring{r}) = \int_{-\mathring{k}_b}^{-\mathring{k}_a} \mathring{F}_1(\mathring{k})\exp(i\mathring{k}\mathring{r})\mathrm{d}\mathring{k} + \int_{\mathring{k}_a}^{\mathring{k}_b} \mathring{F}_1(\mathring{k})\exp(i\mathring{k}\mathring{r})\mathrm{d}\mathring{k}$$
$$= 2\int_{\mathring{k}_a}^{\mathring{k}_b} \mathring{F}_1(\mathring{k})\cos(\mathring{k}\mathring{r})\mathrm{d}\mathring{k},$$
$$g_{ab}(r) = \int_{-\mathring{k}_b}^{-\mathring{k}_a} \mathring{F}_{2,3}(\mathring{k})\exp(i\mathring{k}\mathring{r})\mathrm{d}\mathring{k} + \int_{\mathring{k}_a}^{\mathring{k}_b} \mathring{F}_{2,3}(\mathring{k})\exp(i\mathring{k}\mathring{r})\mathrm{d}\mathring{k}$$
$$= 2\int_{\mathring{k}_a}^{\mathring{k}_b} \mathring{F}_{2,3}(\mathring{k})\cos(\mathring{k}\mathring{r})\mathrm{d}\mathring{k},$$

and due to the fact that the Fourier transform and the sampling transformation (7) are linear transformations, the contribution to the rotational correlation can be expressed by

$$\mathring{R}_{u_{ab}}^{\Omega}(\mathring{\tau};\mathring{\Omega},\mathring{\rho}) = \left[\frac{f_{ab}(\mathring{r}) - g_{ab}(\mathring{r})}{\mathring{r}^2}\mathring{r}_1^2 + g_{ab}(\mathring{r})\right],$$

with $\mathring{r}_1$ and $\mathring{r}$ given by expression (12). $\mathring{R}_{u_{ab}}^{\Omega}(\mathring{\tau};\mathring{\Omega},\mathring{\rho})$ is referred to as the interval limited rotational correlation. The contribution to the rotational spectrum, corresponding to the Eulerian spectrum limited to the frequency interval $[\mathring{f}_a, \mathring{f}_b]$ is the already defined interval limited rotational spectrum given by

$$\mathring{S}_{u_{ab}}^{\Omega}(\mathring{f};\mathring{\Omega},\mathring{\rho}) = 4\int_0^{\infty} \mathring{R}_{u_{ab}}^{\Omega}(\mathring{\tau};\mathring{\Omega},\mathring{\rho})\cos(2\pi\mathring{f}\mathring{\tau})\mathrm{d}\mathring{\tau},\ \mathring{f} \in [0,\infty). \tag{13}$$

The variance associated to the interval limited rotational spectrum, $\mathring{\sigma}^2_{u_{ab}^{\Omega}}$, is defined by

$$\mathring{\sigma}^2_{u_{ab}^{\Omega}} = \int_0^{\infty} \mathring{S}_{u_{ab}}^{\Omega}(\mathring{f},\mathring{\Omega},\mathring{\rho})\mathrm{d}\mathring{f},$$

and using the relationship between spectrum and correlation, this variance can be expressed as

$$\mathring{\sigma}^2_{u_{ab}^{\Omega}} = \lim_{\mathring{\tau}\to 0} \mathring{R}_{u_{ab}}^{\Omega}(\mathring{\tau};\mathring{\Omega},\mathring{\rho}) = \frac{f_{ab}(0) - g_{ab}(0)}{\lambda_\rho^2 + 1} + g_{ab}(0). \tag{14}$$

Note that is

$$\mathring{\sigma}^2_{u_{ab}^{\Omega}} \neq \mathring{\sigma}^2_u\Big|_a^b = \int_{\mathring{f}_a}^{\mathring{f}_b} \mathring{S}_u(\mathring{f})\mathrm{d}\mathring{f} = f_{ab}(0)$$

since $f_{ab}(0) \neq g_{ab}(0)$. This implies that, whereas the variance corresponding to the Eulerian spectrum $\mathring{S}_u^{\Omega}$ equals that of $\mathring{S}_u$, as established in expression (10), this is not the case with the variances $\mathring{\sigma}^2_{u_{ab}^{\Omega}}$ and $\mathring{\sigma}^2_u\Big|_a^b$, corresponding to $\mathring{S}_{u_{ab}}^{\Omega}$, $\mathring{f} \in [0,\infty)$, and $\mathring{S}_u$, $\mathring{f} \in [\mathring{f}_a, \mathring{f}_b]$, respectively.

This not preserving variance transformation is illustrated in Fig. 5 for values $\lambda_\rho = 8.1$ and $\mathring{\rho} = 0.5$. We represent in Fig. 5*a* the Eulerian

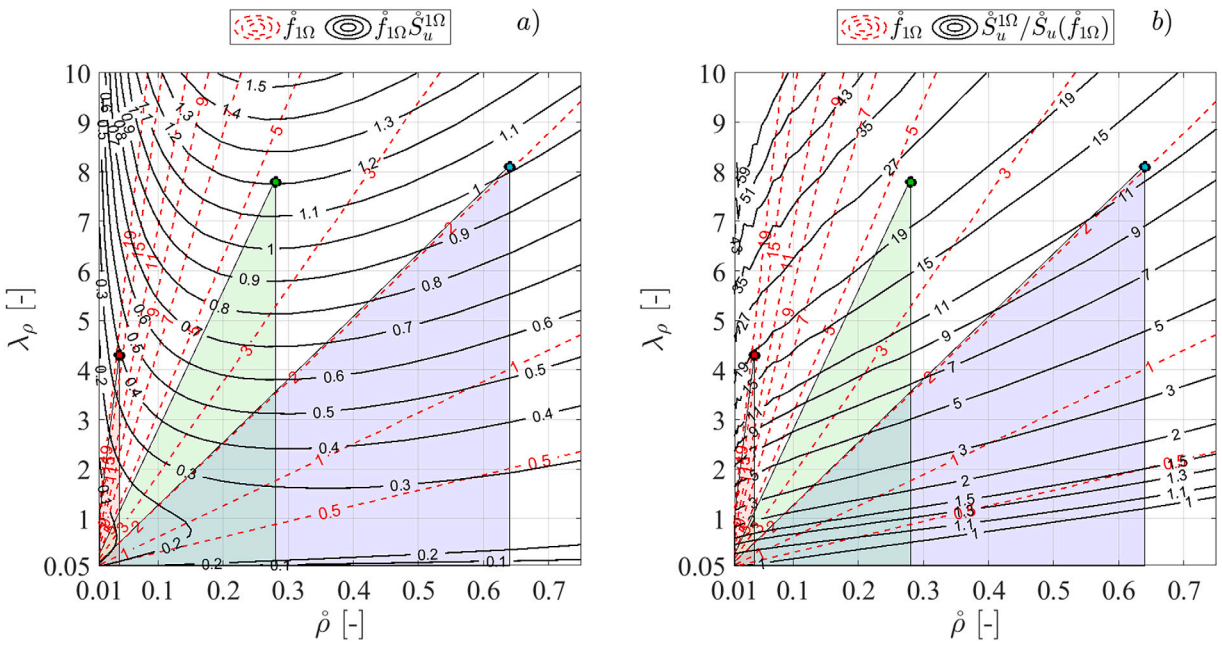

Fig. 3. *a*) Normalized rotational spectrum at 1Ω peak $\mathring{f}_{1\Omega}\mathring{S}_u^{1\Omega}$, *b*) Ratio $\mathring{S}_u^{1\Omega}/\mathring{S}_u(\mathring{f}_{1\Omega})$, versus the radial section speed ratio λ_ρ and radial position $\mathring{\rho}$. The colored areas identify characteristic $\mathring{\rho}-\lambda_\rho$ values of the blade sections of the SSWT (red), the MSWT (green) and the LSWT (blue). The circled markers represent the values from Table 1. (For interpretation of the references to color in this figure legend, the reader is referred to the web version of this article.)

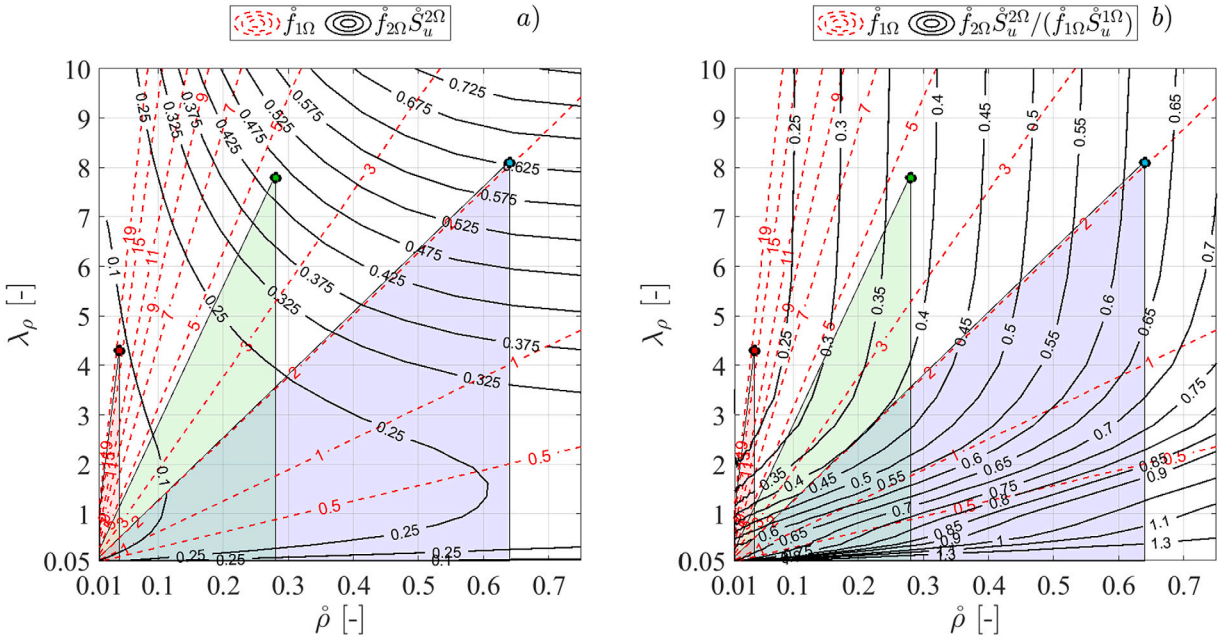

Fig. 4. *a*) Normalized rotational spectrum at 2Ω peak $\mathring{f}_{2\Omega}\mathring{S}_u^{2\Omega}$, *b*) Ratio $\mathring{f}_{2\Omega}\mathring{S}_u^{2\Omega}/(\mathring{f}_{1\Omega}\mathring{S}_u^{1\Omega})$, versus the radial section speed ratio λ_ρ and radial position $\mathring{\rho}$. Color codes as in Fig. 3. (For interpretation of the references to color in this figure legend, the reader is referred to the web version of this article.)

spectrum, $\mathring{S}_u(\mathring{f})$, also included in the rest of the subfigures as reference, and we highlight the part of this spectrum corresponding to a frequency interval $[\mathring{f}_a, \mathring{f}_b]$. This interval is centered in the frequency, $\mathring{f}_{\max}$, which maximizes the normalized Eulerian spectrum $\mathring{f}\mathring{S}_u$ and accounts for 20% of the total variance, that is

$$\mathring{\sigma}_u^2\Big|_a^b = \int_{\mathring{f}_a}^{\mathring{f}_b} \mathring{S}_u(\mathring{f})\mathrm{d}\mathring{f} = 0.2,$$

with $\mathring{f}_a = \mathring{f}_{\max} - \Delta\mathring{f}$, $\mathring{f}_b = \mathring{f}_{\max} + \Delta\mathring{f}$. The gray area under the curve represents the variance, $\mathring{\sigma}_u^2 = \sigma_u^2\sigma_0^{-2} = 1$, whereas the orange area under the curve represents the variance corresponding to the frequency interval $[\mathring{f}_a, \mathring{f}_b]$, $\mathring{\sigma}_u^2\Big|_a^b = \sigma_u^2\Big|_a^b/\sigma_0^2$. In Fig. 5*b* the normalized rotational spectrum $\mathring{f}\mathring{S}_u^{\Omega}$ is represented. The gray area under the curve represents the rotational variance $\mathring{\sigma}_{u\Omega}^2 = \sigma_{u\Omega}^2/\sigma_0^2 = 1$, with $\sigma_{u\Omega}^2$ given by expression (9) or (10), whereas the orange area under the curve represents the rotational variance corresponding to the frequency interval $[\mathring{f}_a, \mathring{f}_b]$, $\mathring{\sigma}_{u\Omega}^2\Big|_a^b$, given by

$$\mathring{\sigma}_{u\Omega}^2\Big|_a^b = \int_{\mathring{f}_a}^{\mathring{f}_b} \mathring{S}_u^{\Omega}(\mathring{f}, \mathring{\Omega}, \mathring{\rho})\mathrm{d}\mathring{f}.$$

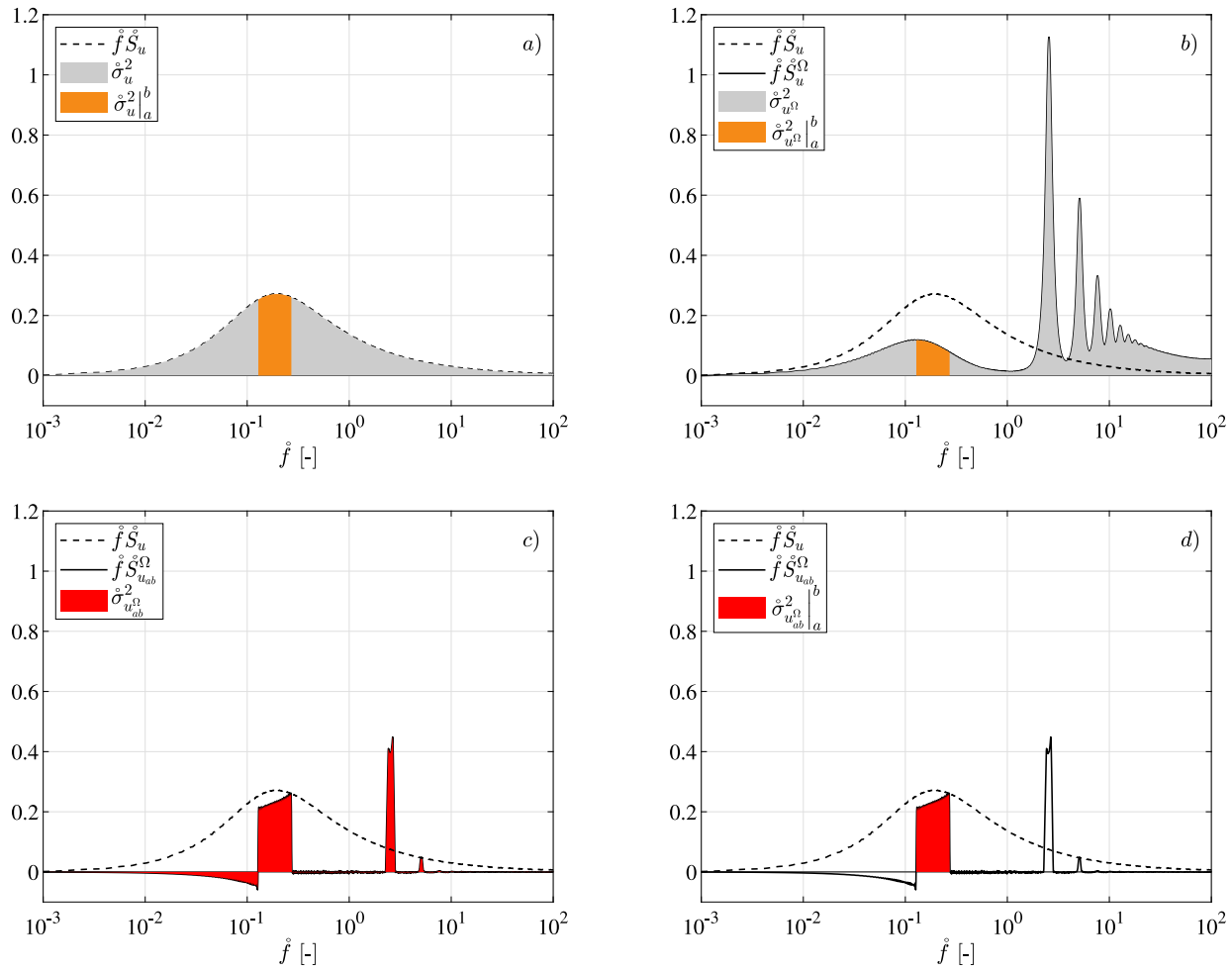

Fig. 5. *a*) Normalized Eulerian spectrum $\mathring{f}\mathring{S}_u$. Variance $\mathring{\sigma}^2_u = \sigma^2_u\sigma_0^{-2}$ and variance corresponding to the frequency interval $[\mathring{f}_a, \mathring{f}_b]$ centered in $\mathring{f}_{\max} = 0.2$ and accounting for variance $\mathring{\sigma}^2_u|^b_a = 0.2$. *b*) Normalized rotational spectrum $\mathring{f}\mathring{S}^{\Omega}_u$, rotational variance $\mathring{\sigma}^2_{u^{\Omega}}$, and rotational variance corresponding to the frequency interval $[\mathring{f}_a, \mathring{f}_b]$, $\mathring{\sigma}^2_{u^{\Omega}}|^b_a$. *c*) Normalized interval limited rotational spectrum $\mathring{f}\mathring{S}^{\Omega}_{u_{ab}}$ and interval limited rotational variance, $\mathring{\sigma}^2_{u^{\Omega}_{ab}}$. *d*) Normalized interval limited rotational spectrum $\mathring{f}\mathring{S}^{\Omega}_{u_{ab}}$ and interval limited rotational variance due to the frequency interval $[\mathring{f}_a, \mathring{f}_b]$, $\mathring{\sigma}^2_{u^{\Omega}_{ab}}|^b_a$. $\lambda_\rho = 8.1$ and $\hat{\rho} = 0.5$. The x axis is plotted using natural logarithm scale. (For interpretation of the references to color in this figure legend, the reader is referred to the web version of this article.)

It is well known (Connell and George, 1987), that $\mathring{\sigma}^2_{u^{\Omega}}|^b_a \neq \mathring{\sigma}^2_u|^b_a$. In Fig. 5*c* the normalized interval limited rotational spectrum $\mathring{f}\mathring{S}^{\Omega}_{u_{ab}}$, with $\mathring{S}^{\Omega}_{u_{ab}}$ given by expression (13), is presented along with the rotational interval limited variance (red area), $\mathring{\sigma}^2_{u^{\Omega}_{ab}}$ given by expression (14). This variance is the contribution to the total rotational variance, of the part of the rotational spectrum, $\mathring{S}^{\Omega}_{u_{ab}}$, which results from the transformation of the part of the Eulerian spectrum, $\mathring{S}_u(\mathring{f})$, corresponding to the frequency interval $[\mathring{f}_a, \mathring{f}_b]$. As mentioned before $\mathring{\sigma}^2_{u^{\Omega}_{ab}} \neq \mathring{\sigma}^2_u|^b_a$ which means that the red area in Fig. 5*c* is not the same as the orange area in Fig. 5*a*. Finally, in Fig. 5*d*, the interval limited rotational variance associated to the frequency interval $[\mathring{f}_a, \mathring{f}_b]$, $\mathring{\sigma}^2_{u^{\Omega}_{ab}}|^b_a$ given by

$$\mathring{\sigma}^2_{u^{\Omega}_{ab}}\Big|^b_a = \int_{\mathring{f}_a}^{\mathring{f}_b} \mathring{S}^{\Omega}_{u_{ab}}(\mathring{f}, \mathring{\Omega}, \hat{\rho})\mathrm{d}\mathring{f},$$

is represented by the red area.

To underline the idea that the variance of the Eulerian spectrum $\mathring{S}_u$ corresponding to frequencies $\mathring{f} \in [\mathring{f}_a, \mathring{f}_b]$, is not conserved in the normalized interval limited rotational spectrum $\mathring{f}\mathring{S}^{\Omega}_{u_{ab}}$, $\mathring{f} \in [0, \infty)$, the ratio $\mathring{\sigma}^2_{u^{\Omega}_{ab}} / \mathring{\sigma}^2_u|^b_a$ is written from expression (14) as

$$\mathring{\sigma}^2_{u^{\Omega}_{ab}} / \mathring{\sigma}^2_u|^b_a = \left(\frac{f_{ab}(0) - g_{ab}(0)}{1+\lambda_\rho^2} + g_{ab}(0)\right) f_{ab}^{-1}(0) = \frac{1 - \dfrac{g_{ab}(0)}{f_{ab}(0)}}{1+\lambda_\rho^2} + \frac{g_{ab}(0)}{f_{ab}(0)} = \\ = \frac{1}{1+\lambda_\rho^2}\left(1 + \lambda_\rho^2 \frac{g_{ab}(0)}{f_{ab}(0)}\right). \quad (15)$$

The expression (15) is represented in Fig. 6 for a range of frequency intervals $[\mathring{f}_{a_i}, \mathring{f}_{b_i}] = [\mathring{f}_i - \Delta\mathring{f}, \mathring{f}_i + \Delta\mathring{f}]$ so that $\mathring{\sigma}^2_u|^b_a = 0.15$.

Therefore, for frequency intervals $[\mathring{f}_a, \mathring{f}_b]$ centered at values $\mathring{f}_i > \mathring{f}_i{}^*$, where $\mathring{f}_i{}^*$ which corresponds to $f_{ab^*}(0) = g_{ab^*}(0)$, see Fig. 6, is $g_{ab}(0) > f_{ab}(0)$ and therefore $\mathring{\sigma}^2_{u^{\Omega}_{ab}} > \mathring{\sigma}^2_u|^b_a$, so, for those frequency intervals, the rotational sampling process amplifies the variance of the original part of the Eulerian spectrum. For intervals centered at frequencies $\mathring{f}_i < \mathring{f}_i{}^*$ is $g_{ab}(0) < f_{ab}(0)$ and $\mathring{\sigma}^2_{u^{\Omega}_{ab}} < \mathring{\sigma}^2_u|^b_a$.

We extend now the analysis of Fig. 5 to different intervals $[\mathring{f}_{a_i}, \mathring{f}_{b_i}]$ and different λ_ρ values. Six consecutive and non overlapping intervals $[\mathring{f}_{a_i}, \mathring{f}_{b_i}]$ have been considered with the same variance $\mathring{\sigma}^2_u|^b_a$. In Fig. 7, the interval limited correlation function at a fixed point, $\mathring{R}_{u_{ab,i}}(\mathring{\tau}) =$

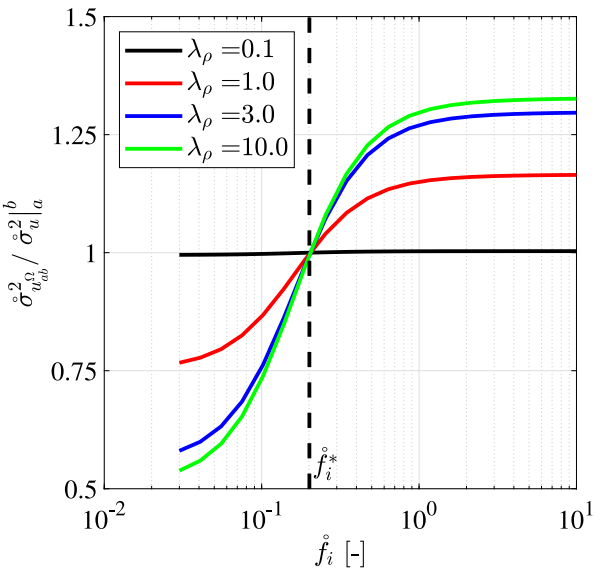

Fig. 6. Ratio of interval limited rotational variance $\mathring{\sigma}^2_{u^\Omega_{ab}}$ and the variance corresponding to different frequency intervals $[\mathring{f}_{a_i}, \mathring{f}_{b_i}]$ of the Eulerian spectrum centered at frequencies $\mathring{f}_i \in [0.03, 10]$ and accounting for a variance $\mathring{\sigma}^2_u\big|^b_a = 0.15$. The results are presented for different values of the radial section speed ratio λ_ρ and a radial position $\hat{\rho} = 0.5$. The value of the central frequency $\mathring{f}_i^*$ which gives rise to $f_{ab}(0) = g_{ab}(0)$ is indicated in the figure. (For interpretation of the references to color in this figure legend, the reader is referred to the web version of this article.)

$f_{ab,i}(\mathring{r} = \mathring{\tau})$, and the interval limited rotational correlation $\mathring{R}^\Omega_{u_{ab,i}}(\mathring{\tau}; \mathring{\Omega}, \mathring{\rho})$, both corresponding to the frequency interval $[\mathring{f}_{a_i}, \mathring{f}_{b_i}]$ are plotted for frequency intervals $[\mathring{f}_{a_i}, \mathring{f}_{b_i}]$ centered in $\mathring{f}_i = 0.03, 0.08, 0.16, 0.28, 0.57$, and 1.97, each of them accounting for a variance $\mathring{\sigma}^2_u\big|^b_a = 0.15$. The correlation function at a fixed point $\mathring{R}_u(\mathring{\tau})$ and the rotational correlation, $\mathring{R}^\Omega_u(\mathring{\tau}; \mathring{\Omega}, \hat{\rho})$ are presented in every subfigure to facilitate the comparison.

Both the interval limited correlation, $\mathring{R}_{u_{ab}}$ and interval limited rotational correlation $\mathring{R}^\Omega_{u_{ab}}$, are significantly different depending on the frequency interval considered. Intervals of time delay $\mathring{\tau}$ with positive and negative contributions to the respective correlation functions $\mathring{R}_u$ and $\mathring{R}^\Omega_u$ are observed.

The corresponding normalized interval limited rotational spectra are presented in Figs. 8–10 for the three wind turbine cases on Table 1.

In the SSWT case (Fig. 8), the rotational sampling effect is noticeable, although less intense that in the other two cases. The energy of the interval limited rotational spectrum associated to the frequency interval $[\mathring{f}_{a_i}, \mathring{f}_{b_i}]$ is quite similar to the energy of the Eulerian spectrum in the frequency interval $[\mathring{f}_{a_i}, \mathring{f}_{b_i}]$. Each frequency interval contributes in a different way to the rotational spectrum for frequencies outside the frequency interval $[\mathring{f}_{a_i}, \mathring{f}_{b_i}]$ and specifically at the $n\Omega$ peaks regions. In the cases of MSWT and LSWT, the energy associated to the interval limited rotational spectrum corresponding to the frequency interval $[\mathring{f}_{a_i}, \mathring{f}_{b_i}]$ clearly differs from the energy of the Eulerian spectrum in the frequency interval $[\mathring{f}_{a_i}, \mathring{f}_{b_i}]$. The mentioned differences increase as the frequency interval $[\mathring{f}_{a_i}, \mathring{f}_{b_i}]$ is closer to the rotation frequency, as in figures 9.e and 9.f or in figures 10.d, 10.e and 10.f. In these cases, the region of the Eulerian spectrum corresponding to the frequency interval $[\mathring{f}_{a_i}, \mathring{f}_{b_i}]$ is transformed into a contribution to the rotational spectrum presenting negative values for frequencies $\mathring{f} < \mathring{f}_{a_i}$. These negative values indicate that the fluctuations of the original velocity field corresponding to frequencies $[\mathring{f}_{a_i}, \mathring{f}_{b_i}]$, when sampled by the rotating point, lead to a sampled velocity contribution which is negatively correlated for certain frequency intervals, giving rise to the aforementioned negative contributions to the rotational spectrum. These

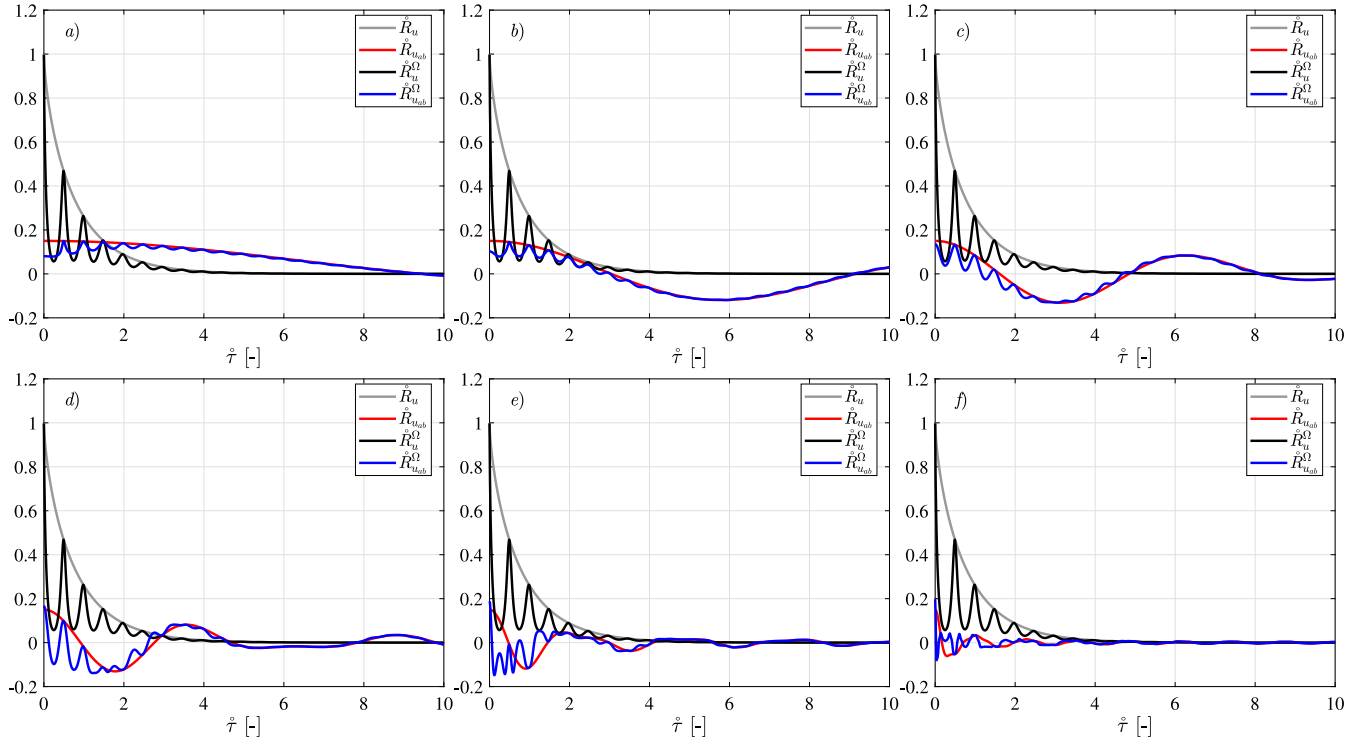

Fig. 7. Correlation function at a fixed point $\mathring{R}_u$, interval limited correlation function at a fixed point corresponding to the frequency interval $[\mathring{f}_{a_i}, \mathring{f}_{b_i}]$, $\mathring{R}_{u_{ab}}$, rotational correlation $\mathring{R}^\Omega_u$ and interval limited rotational correlation $\mathring{R}^\Omega_{u_{ab}}$, for intervals $[\mathring{f}_{a_i}, \mathring{f}_{b_i}]$ centered in $\mathring{f}_i = 0.03\,(a)$, $0.08\,(b)$, $0.16\,(c)$, $0.28\,(d)$, $0.57\,(e)$ and $1.97\,(f)$, each of them accounting for $\mathring{\sigma}^2_u\big|^b_a = 0.15$. Analysis for the LSWT described in Table 1. (For interpretation of the references to color in this figure legend, the reader is referred to the web version of this article.)

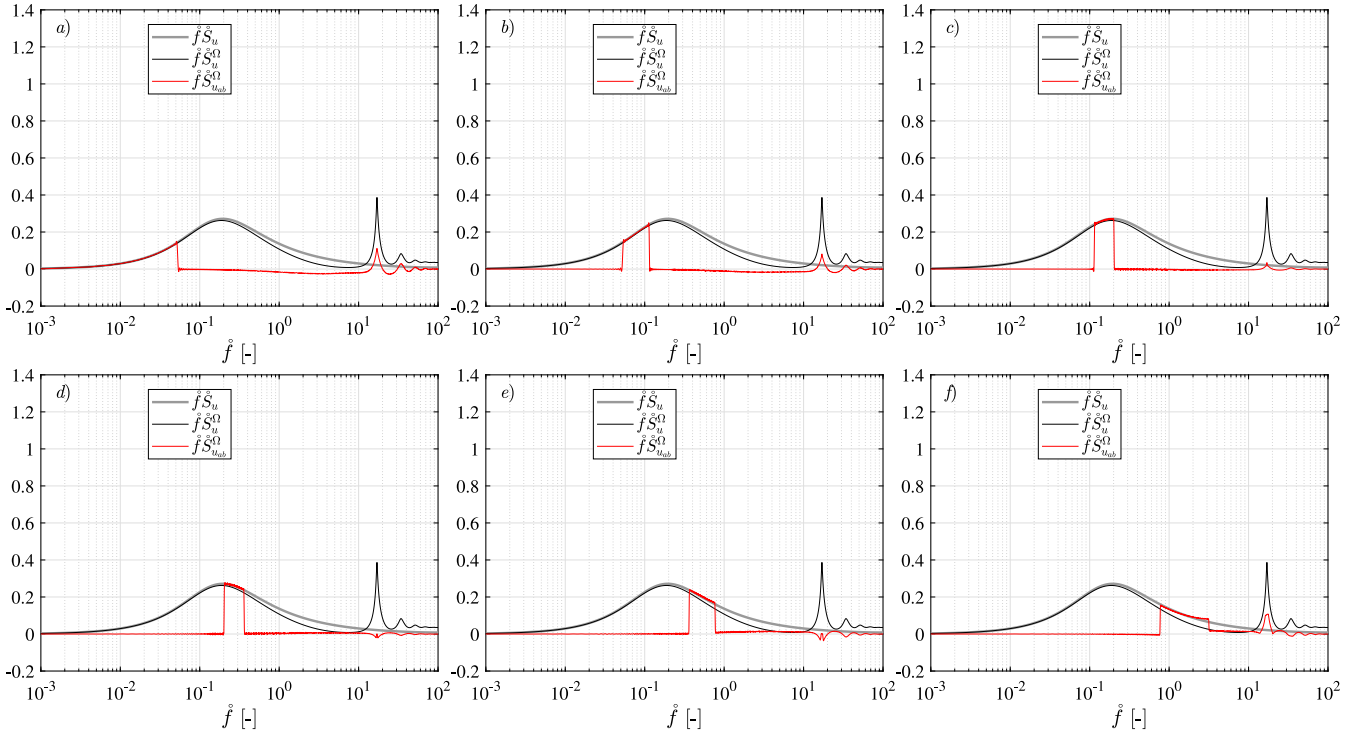

Fig. 8. Normalized Eulerian longitudinal spectrum $\mathring{f}\mathring{S}_u$, normalized rotational spectrum $\mathring{f}\mathring{S}_u^{\Omega}$ and normalized interval limited rotational spectrum $\mathring{f}\mathring{S}_{u_{ab}}^{\Omega}$ for intervals centered in $\mathring{f}_i = 0.03\,(a)$, $0.08\,(b)$, $0.16\,(c)$, $0.28\,(d)$, $0.57\,(e)$ and $1.97\,(f)$, accounting each of them for $\hat{\sigma}_u^2|_a^b = 0.15$. Analysis for the SSWT described in Table 1. (For interpretation of the references to color in this figure legend, the reader is referred to the web version of this article.)

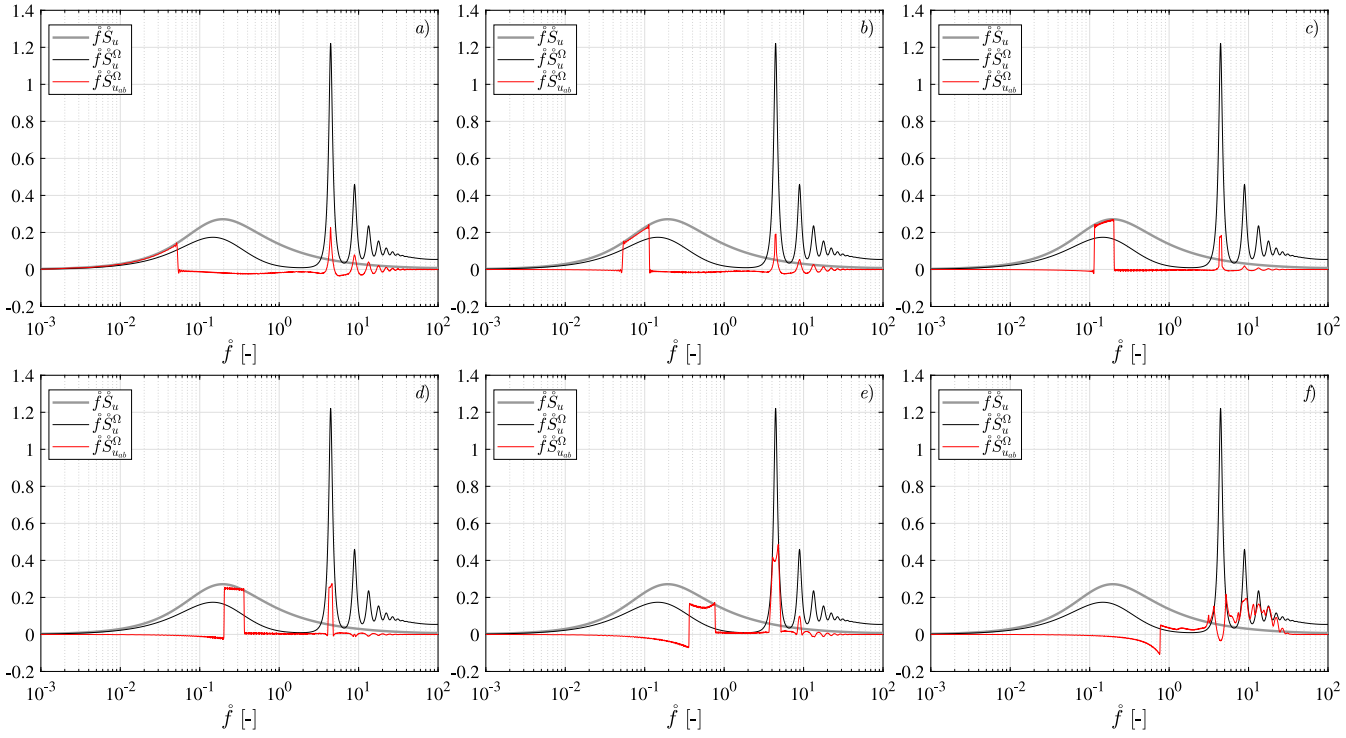

Fig. 9. As in Fig. 8. Analysis for the MSWT described in Table 1. (For interpretation of the references to color in this figure legend, the reader is referred to the web version of this article.)

negative contributions appear also in part of the $n\Omega$ peaks regions. In the case of the higher frequency intervals $[\mathring{f}_{a_i}, \mathring{f}_{b_i}]$, the contributions to the 1Ω peak are clearly negative for both the MSWT and LSWT cases, as can be seen in figures 9.f, 10.f and 10.g. In these cases, the energy contained in the corresponding frequency interval $[\mathring{f}_{a_i}, \mathring{f}_{b_i}]$ of the Eulerian spectrum is not displaced to the 1Ω peak region of

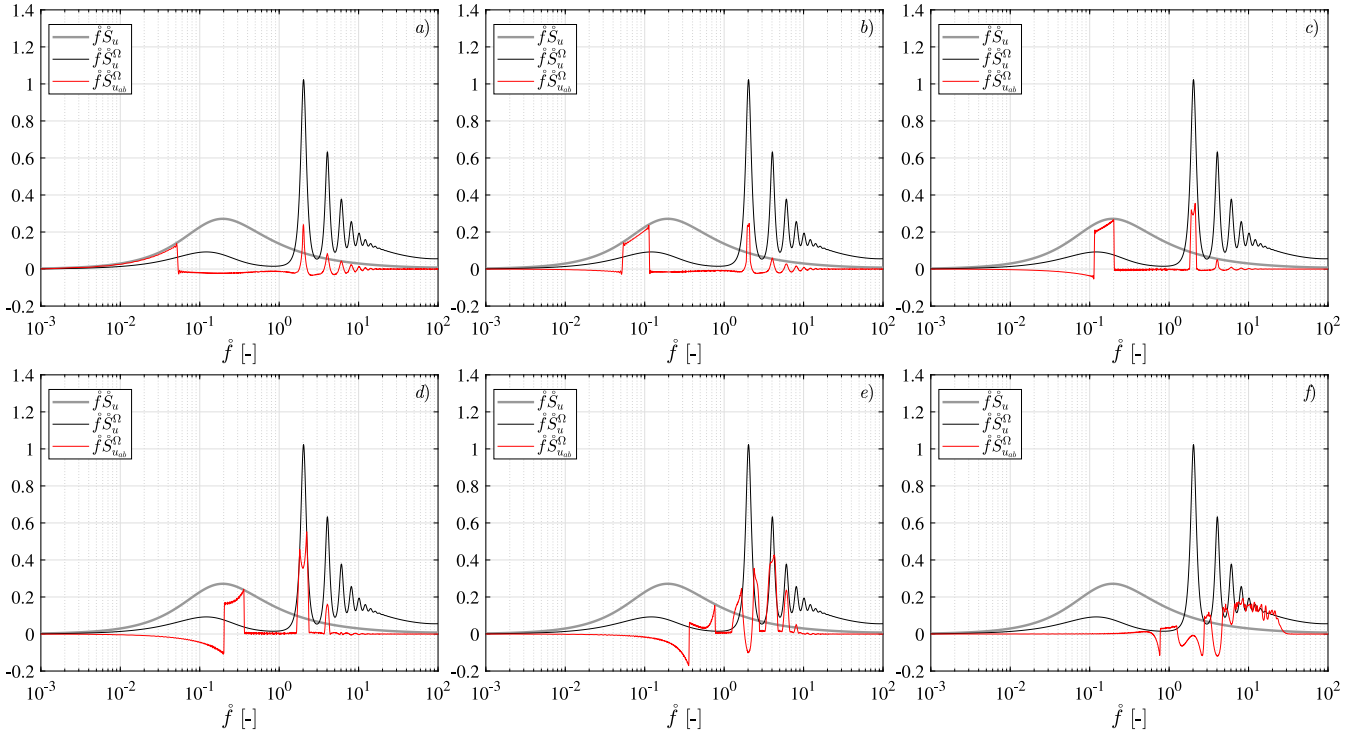

Fig. 10. As in Fig. 8. Analysis for the LSWT described in Table 1. (For interpretation of the references to color in this figure legend, the reader is referred to the web version of this article.)

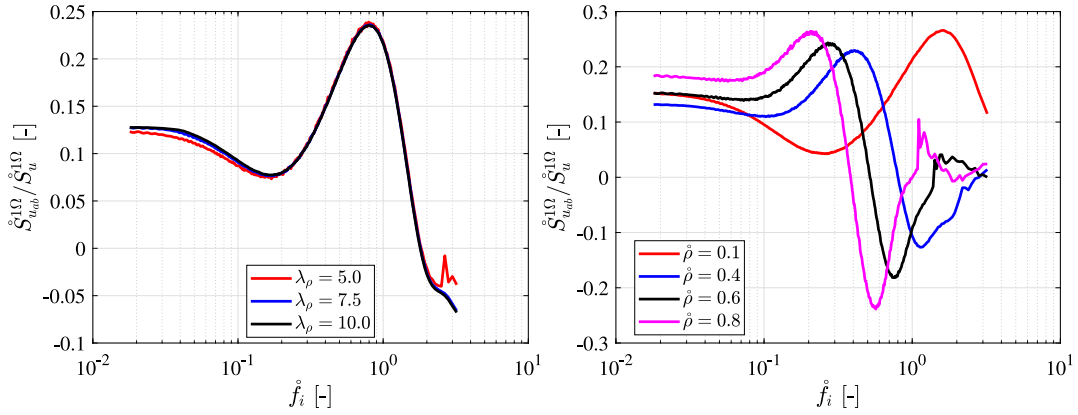

Fig. 11. Ratio $\mathring{S}_{u_{ab}}^{\Omega}/\mathring{S}_u^{\Omega}$ at $\mathring{f} = \mathring{f}_{1\Omega} = \mathring{\Omega}(2\pi)^{-1}$, versus the central frequency of the interval $[\mathring{f}_{a_i}, \mathring{f}_{b_i}]$, $\mathring{f}_i = 0.5(\mathring{f}_{a_i} + \mathring{f}_{b_i})$ accounting for a variance $\mathring{\sigma}_u^2\big|_a^b = 0.1$. Left: for different values of λ_ρ and a radial position $\mathring{\rho} = 0.2$. Right: for different values of $\mathring{\rho}$ and a value $\lambda_\rho = 7.5$. (For interpretation of the references to color in this figure legend, the reader is referred to the web version of this article.)

the rotational spectrum but instead, it is transformed into a negative contribution to the rotational peak. Further analysis of this mechanism is ongoing by exploring how different wave number components of the velocity field are sampled by the rotating point.

The contributions to the first rotational peak of the interval limited rotational spectra, $\mathring{f}_{1\Omega}\mathring{S}_{u_{ab}}^{1\Omega}$ are presented in Fig. 11 for different values of parameters $\mathring{\rho}$ and λ_ρ. The ratio $\mathring{S}_{u_{ab}}^{1\Omega}/\mathring{S}_u^{1\Omega}$ is presented for overlapping frequency intervals centered in $\mathring{f}_i \in [0.2 \cdot 10^{-2}, 3]$ and accounting for interval limited variance $\mathring{\sigma}_u^2\big|_a^b = 0.1$ each of them. This ratio changes significantly with the central frequency, $\mathring{f}_i$, being even negative for certain $\mathring{f}_i$ values. This means that the energy from the different frequency intervals $[\mathring{f}_a, \mathring{f}_b]$ of the Eulerian spectra, $\mathring{S}_u$, with identical variance $\mathring{\sigma}_u^2\big|_a^b$, is shifted in a significantly different way to the first rotational peak region, even giving rise to a negative contribution to the mentioned first peak, as it was anticipated in Figs. 9 and 10.

5. Conclusions

We have used a classical model of rotational sampling of statistically stationary, homogeneous and isotropic turbulence to extend the analysis of the characteristics of the rotational spectra to ranges of non dimensional radial position of the rotating point and non dimensional rotational speed.

We have proved that the transformation of the interval limited Eulerian spectrum into the interval limited rotational spectrum does not preserve the variance (as it occurs with the transformation of the whole Eulerian spectrum into the rotational spectrum). The change of variance depends on the relative contribution of longitudinal and transversal correlation functions. The product of the non dimensional radial position and non dimensional rotational speed has been identified as the parameter driving this non preserving transformation of variances.

We have explicitly shown that different frequency intervals of the Eulerian spectrum are transformed into significantly different contributions along the whole frequency interval of the rotational spectrum, and especially into significantly different contributions to the first and second rotational peaks. The interval limited rotational spectrum can be even negative along certain frequency intervals, including those corresponding to the first and second rotational peaks. This means that certain frequency components of the original velocity field can be negatively correlated when sampled by the rotating point, giving rise to the aforementioned negative contributions.

The presented analysis can help in the analysis of wind turbine response to turbulence since, in the line of Chen et al. (2020), allows to know how different frequency regions of the Eulerian spectrum contribute to those frequency regions of the rotational spectrum where the wind turbine is specially sensitive. With this regard, the presented results constitute a starting point for a future analysis on how each part of the Eulerian wind spectrum contributes to the spectral characteristics of the dynamic response of wind turbine rotating blades, such as the blade tip displacement spectrum or the blade root bending moment spectrum, along the whole frequency interval (including the rotational peaks frequency regions and the frequency regions around the blade natural frequencies). This analysis is ongoing and constitutes a piece of research itself since it requires, first: to extend the same frequency interval analysis that has been applied to the one point spectrum herein, to the two points cross-spectrum (coherence function), second: to apply a proper aeroelastic model for the rotating blade such an Euler Bernoulli beam model for the structural behavior of the rotating blade and a blade element momentum model for reproducing the aerodynamic forces on the blade.

CRediT authorship contribution statement

A. Cuerva-Tejero: Supervision, Funding acquisition, Conceptualization, Methodology, Writing - original draft. **M. Rodríguez-Correa:** Methodology, Software. **C. Gallego-Castillo:** Writing - original draft. **O. Lopez-Garcia:** Funding acquisition, Writing - original draft. **S. Ávila-Sánchez:** Software, Writing - original draft. **R. Fernández-Aldama:** Software.

Declaration of competing interest

The authors declare that they have no known competing financial interests or personal relationships that could have appeared to influence the work reported in this paper.

Acknowledgments

This research has been undertaken as a part of the Project MEDEA RTI2018-095592-B-I00, supported by the Spanish Ministry of Research and Innovation under the call 2018 of R&D projects “Research Challenges” of the Spanish State R&D Program Oriented to the Challenges of the Society, 2017–2020.

References

Akins, R.E., 1983. Rotationally-Sampled Flow-Field Measurements for Vertical-Axis Wind Turbines. Tech. Rep. SAND-82-2341C; CONF-830432-2 ON: DE83009550, Sandia National Laboratories, Albuquerque, NW 87185, Presented at the University of Missouri-Columbia Wind/Solar Energy Technology Conference, Kansas City, Missouri. Wind Energy Research Division.

Baker, C.J., 2010. The simulation of unsteady aerodynamic cross wind forces on trains. J. Wind Eng. Ind. Aerodyn. 98, 88–99. http://dx.doi.org/10.1016/j.jweia.2009.09.006.

Bei, C., Zili, Z., Xugang, H., Søren R.K., N, Biswajit, B, 2018. Enhancement of flutter stability in wind turbines with a new type of passive damper of torsional rotation of blades. J. Wind Eng. Ind. Aerodyn. 173, 171–179. http://dx.doi.org/10.1016/j.jweia.2017.12.011.

Burlibaşa, A., Ceangă, E., 2013. Rotationally sampled spectrum approach for simulation of wind speed turbulence in large wind turbines. Appl. Energy 111, 624–635. http://dx.doi.org/10.1016/j.apenergy.2013.05.002.

Burton, T., Sharpe, N., Bossanyi, E., 2001. Wind Energy Handbook. John Wiley and Sons Chichester.

Chen, J., Song, Y., Peng, Y, Sø ren, R.K.N., Zhang, Z., 2020. An efficient rotational sampling method of wind fields for wind turbine blade fatigue analysis. Renew. Energy 146, 2170–2187. http://dx.doi.org/10.1016/j.renene.2019.08.015.

Chen, J., Yang, R., Ma, R., 2015. Wind field simulation of large horizontal-axis wind turbine system under different operating conditions. Struct. Des. Tall Special Build. 24, 973–988. http://dx.doi.org/10.1002/tal.1221.

Connell, J.R., 1981. Spectrum of Wind Speed Fluctuations Encountered by a Rotating Blade of a Wind Energy Conversion System: Observations and Theory. Tech. Rep. PNL-4083 ON: DE82006019, Battelle Pacific Northwest Labs. (USA), http://dx.doi.org/10.2172/5348174, URL https://www.osti.gov/biblio/5348174.

Connell, J.R., 1982. The spectrum of wind speed fluctuations encountered by a rotating blade of a wind energy conversion system. Sol. Energy 29 (5), 363–375. http://dx.doi.org/10.1016/0038-092X(82)90072-X.

Connell, J.R., 1988. A primer of turbulence at the wind turbine rotor. Sol. Energy 41, 281–293. http://dx.doi.org/10.1016/0038-092x(88)90146-6.

Connell, J.R., 1995. Basic principles and recent observations of rotationally sampled wind. In: NASA STI. DASCON Engineering, Collected Papers on Wind Turbine Technology. Pacific Northwest Lab., Richland, WA (USA).

Connell, J.R., George, R.L., 1987. Accurate correlation of wind turbine response with wind speed using a new characterization of turbulent wind. J. Sol. Energy Eng. 109, 321. http://dx.doi.org/10.1115/1.3268224.

Connell, J.R., Morris, V.R., 1989. Rotationally Sampled Wind Characteristics for Several Rotor Sizes Using Laser Anemometer Measurements. Tech. Rep. PNL-6811 ON: DE89007942, Pacific Northwest Lab., Richland, WA (USA), http://dx.doi.org/10.2172/6221452, URL https://www.osti.gov/biblio/6221452.

Connell, J.R., Powell, D.C., 1989. Comparison of measured and modeled turbulence spectra for a point rotating as on a horizontal-axis wind turbine. J. Sol. Energy Eng. 111, 268. http://dx.doi.org/10.1115/1.3268321.

Cooper, R.K., 1984. Atmospheric turbulence with respect to moving ground vehicles. J. Wind Eng. Ind. Aerodyn. 17, 215–238. http://dx.doi.org/10.1016/0167-6105(84)90057-6.

Costello, M, Gaonkar, G.H., Prasad, J.V.R., Schrage, D.P., 1992. Some issues on modeling atmospheric turbulence experienced by helicopter rotor blades. J. Am. Helicopter Soc. 37, 71–75. http://dx.doi.org/10.4050/jahs.37.71.

Dragt, J.B., 1990. Atmospheric turbulence characteristics in the rotating frame of reference of a WECS rotor. In: Proc. European Community Wind Energy Conf, pp. 274–278.

Durbin, P.A., Reif, B.A.P., 2011. Statistical Theory and Modeling for Turbulent Flows, Ed. 2 Wiley Online Library.

Elgammi, M., Sant, T., Alshaikh, M., 2020. Predicting the stochastic aerodynamic loads on blades of two yawed downwind hawts in uncontrolled conditions using a bem algorithm. Renew. Energy 146, 371–383. http://dx.doi.org/10.1016/j.renene.2019.06.114.

Eliassen, L., Jakobsen, J., Krokstad, J., 2015. The effect of turbulent wind field on loads of a wind turbine rotor of increasing size. In: 14th International Conference on Wind Engineering, Porto Alegre, Brazil.

Fluck, M., Crawford, C., 2016. Minimizing errors in interpolated discrete stochastic wind fields. J. Wind Eng. Ind. Aerodyn. 152, 15–22. http://dx.doi.org/10.1016/j.jweia.2016.02.007, URL https://www.sciencedirect.com/science/article/pii/S0167610516300940.

Gaonkar, G.H., 2008. Review of turbulence modeling and related applications to some problems of helicopter flight dynamics. J. Am. Helicopter Soc. 53, 87. http://dx.doi.org/10.4050/jahs.53.87.

George, R.L., 1984. Simulation of Winds as Seen by a Rotating Vertical Axis Wind Turbine Blade. Tech. Rep. PNL-4914 ON: DE84009033, Pacific Northwest Lab., Richland, WA (USA), http://dx.doi.org/10.2172/5224413, URL https://www.osti.gov/biblio/5224413.

George, R.L., Connell, J.R., 1984. Rotationally Sampled Wind Characteristics and Correlations with MOD-OA Wind Turbine Response. Tech. Rep. PNL-5238 ON: DE85001770, Pacific Northwest Lab., Richland, WA (USA), http://dx.doi.org/10.2172/6596575, URL https://www.osti.gov/biblio/6596575.

Hardesty, R.M., Weber, B.F., 1986. Lidar measurement of turbulence encountered by horizontal-axis wind turbines. J. Atmos. Ocean. Technol. 4 (1), 191–203. http://dx.doi.org/10.1175/1520-0426(1987)004<0191:LMOTEB>2.0.CO;2.

Jonkman, J., Butterfield, S., Musial, W., Scott, G., 2009. Definition of a 5-MW reference wind turbine for offshore system development. Tech. Rep. NREL/TP-500-38060, National Renewable Enery Laboratory.

von Karman, T., 1948. Progress in the statistical theory of turbulence. Proc. Natl. Acad. Sci. 34, 530–539. http://dx.doi.org/10.1073/pnas.34.11.530.

Kristensen, L., 1983. Power spectra and cross-spectra as seen from the moving blade of a wind turbine. J. Wind Eng. Ind. Aerodyn. 12, 245–250. http://dx.doi.org/10.1016/0167-6105(83)90073-9.

Kristensen, L., Frandsen, S.T., 1982. Model for power spectra of the blade of a wind turbine measured from the moving frame of reference. J. Wind Eng. Ind. Aerodyn. 10 (2), 249–262. http://dx.doi.org/10.1016/0167-6105(82)90067-8.

Mann, J., 1994. Models in Micrometeorology. Tech. Rep. R-727(EN), RISØ National Laboratory, Roskilde, Denmark.

Murtagh, P.J., Basu, B., Broderick, B.M., 2005. Along-wind response of a wind turbine tower with blade coupling subjected to rotationally sampled wind loading. Eng. Struct. 27, 1209–1219. http://dx.doi.org/10.1016/j.engstruct.2005.03.004.

Napolitano, A., 2012. Generalizations of Cyclostationary Signal Processing: Spectral Analysis and Applications. Wiley-IEEE Press.

Petersen, J.T., Kretz, A., Mann, J., 1994. Influence of transversal turbulence on lifetime predictions for a HAWT. In: European Wind Energy Conference and Exhibition, EWEC '94, 10-14 October 1994, Thessaloniki, Macedonia, Greece.

Pope, S.B., 2000. Turbulent Flows. Cambridge University Press, Cambridge, UK.

Powell, D.C., Connell, J.R., 1986. Review of Wind Simulation Methods for Horizontal-Axis Wind Turbine Analysis. Tech. Rep. PNL-5903 ON: DE86012223, Pacific Northwest Lab., Richland, WA (USA), http://dx.doi.org/10.2172/5594885, URL https://www.osti.gov/biblio/5594885.

Powell, D.C., Connell, J.R., 1987. Verification of theoretically computed spectra for a point rotating in a vertical plane. Sol. Energy 39, 53–63. http://dx.doi.org/10.1016/s0038-092x(87)80051-8.

Riaz, J., Prasad, J.V.R., Schrage, D.P., Gaonkar, G.H., 1993. Atmospheric turbulence simulation for rotorcraft applications. J. Am. Helicopter Soc. 38, 84. http://dx.doi.org/10.4050/JAHS.38.84.

Rosenbrock, H.H., 1955. Vibration and Stability Problems in Large Wind Turbines Having Hinged Blades. Tech. Rep. C/T113, British Electrical and Allied Industries Research Association.

Sandborn, V.A., Connell, J.R., 1984. Measurement of Turbulent Wind Velocities Using a Rotating Boom Apparatus. Tech. Rep. PNL-4888 ON: DE84012417, Pacific Northwest Lab., Richland, WA (USA); Colorado State Univ., Fort Collins (USA), http://dx.doi.org/10.2172/6906186, URL https://www.osti.gov/biblio/6906186.

Sekar, A., Padmanabhan, K., Rott, A., van Dooren, M.F., Kühn, M., 2020. How much flow information can a turbine-mounted lidar capture? J. Phys. Conf. Ser. 1618 (3).

Simley, E., Pao, L., 2013. Correlation between rotating LIDAR measurements and blade effective wind speed. In: 51st AIAA Aerospace Sciences Meeting Including the New Horizons Forum and Aerospace Exposition. American Institute of Aeronautics and Astronautics, http://dx.doi.org/10.2514/6.2013-749.

Sørensen, P., Hansen, A.D., Carvalho-Rosas, P.A., 2002. Wind models for simulation of power fluctuations from wind farms. J. Wind Eng. Ind. Aerodyn. 90, 1381–1402. http://dx.doi.org/10.1016/s0167-6105(02)00260-x.

Spera, D.A., 1995. A Model of Rotationally-Sampled Wind Turbulence for Predicting Fatigue Loads in Wind Turbines. NASA STI/Recon Technical Report N, Tech. Rep. SEE N95-27970 09-44, pp. 17–26, URL https://ui.adsabs.harvard.edu/abs/1995STIN...9527972S.

Su, Y., Li, M., Yang, Y., Mann, J., Liao, H., Li, X., 2020. Experimental investigation of turbulent fluctuation characteristics observed at a moving point under crossflows. J. Wind Eng. Ind. Aerodyn. 197, 104079. http://dx.doi.org/10.1016/j.jweia.2019.104079, URL https://www.sciencedirect.com/science/article/pii/S0167610519306804.

Taylor, G.I., 1938. The spectrum of turbulence. Proc. Math. Phys. Eng. Sci. 164, 476–490. http://dx.doi.org/10.1098/rspa.1938.0032.

Veers, Paul S., 1988. Three-Dimensional Wind Simulation. Tech. Rep. SAND88-0152, Sandia Laboratories.

Verholek, M.G., 1978. Preliminary Results of a Field Experiment to Characterize Wind Flow Through a Vertical Plane. Tech. Rep. PNL-2518, Battelle Pacific Northwest Labs., http://dx.doi.org/10.2172/6722047, URL https://www.osti.gov/biblio/6722047.